Academic Journal of Science and Technology
ISSN: 2771-3032 | Vol. 17, No. 2, 2025

Study on Impact and Wear Properties of ZGMn13 High Manganese Steel Materials under Dry, Sand and Water Conditions

Xiangpeng Pu [1], Lei Ma [1, *], Yuchen Lou [1], Yue Hu [2], Wen Zhong [1], Heng Xiao [1]

[1] School of Mechanical Engineering, Key Laboratory of Fluid and Power Machinery, Ministry of Education, Xihua University, Chengdu, Sichuan, 610039, China
[2] Aviation Engineering College Civil Aviation Flight University of China, Chengdu, Sichuan, 641400, China
*** Corresponding author:** Lei Ma

Abstract: In this research, an MLD-10 Load Abrasive Wear Testing Machine was used to conduct experiments on ZGMn13, which are common material in mining and agriculture. The tests were conducted at different impact energies (1J, 2J, 3J), respectively, using three experimental groups: dry impact, quartz sand, and water. The findings ZGMn13 high manganese steel exhibits lower wear resistance at an energy of 1J, while at 3J, its wear resistance is the best. Under the same impact energy, the sand addition group exhibits the most severe wear, followed by the water addition group, while the control group demonstrates the least wear. Scanning electron microscopy (SEM) observations reveal distinct wear features on the surface, including ploughing grooves, pits, and spalling. Surface profile analysis and hardness testing further confirm the relationship between wear severity and experimental conditions, while also elucidating the hardening behavior of high-manganese steel during impact. This study provides critical experimental evidence for the application of high-manganes esteel materials in impact-abrasive environments. The surface affected by quartz sand abrasive is rough and uneven, displaying traces of repeated pitting deformation.

Keywords: Impact Wear; Work Hardening; Ploughing Grooves; Pits; Spalling.

1. Introduction

High Manganese Steel (HMS), particularly ZGMn13, is widely recognized for its exceptional work-hardening capacity, high toughness, and superior wear resistance under impact loading conditions [1]. These properties make it a critical material for equipment in industries involving heavy abrasion and dynamic stresses, such as mining machinery, railway crossings, agricultural plows, and crusher components [2]. The unique metastable austenitic microstructure of ZGMn13 enables its transformation into martensite under mechanical deformation, granting it high work-hardening capability and impact toughness [3-6]. In studies by Xu Yunhua [7], it was discovered that in addition to twin-induced hardening, dynamic strain aging, and Fe-Mn-C atomic cluster segregation mechanisms, the presence of microcrystalline and amorphous structures constitutes a significant mechanism for the work hardening of high manganese steel under high-energy impact loading. However, despite its practical relevance, the performance of ZGMn13 in complex service environments such as dry friction, water-lubricated, or sand-abrasion conditions remains insufficiently understood.

The wear behavior of materials is inherently influenced by external factors, including load magnitude, sliding speed, temperature, and environmental media. For ZGMn13, which is often exposed to multiphase environments like wet ore processing or desert mining, understanding the synergistic effects of impact energy and abrasive media is crucial for optimizing its service life. Previous research has primarily focused on dry or lubricated sliding wear. For instance, Fang Qiwen and colleagues systematically investigated the tribological properties and rolling contact fatigue mechanisms of high-speed steel using a dual-disc friction-wear testing system [8]. Their experimental results revealed that under rolling-sliding composite loading, the hardened surface layer of high manganese steel exhibits significant cyclic strengthening effects. The microstructure undergoes cumulative evolution during sustained plastic deformation, ultimately leading to material spalling and the formation of typical fatigue damage characteristics [9]. This study elucidated the damage evolution mechanisms of high manganese steel under coupled mechanical conditions from a micromechanical perspective, providing critical theoretical foundations for service life prediction and fatigue-resistant design. However, research on the combined impact-abrasion mechanisms under water or sand-containing conditions remains limited. For example, H. Engqvist [10] demonstrated through tests on cemented carbides and ceramics under dry friction and water-lubricated conditions that water lubrication reduces friction, while acidic aqueous environments further lower friction but accelerate wear rates due to corrosion of the binder phase. P.C. Machado [11] investigated the abrasive wear of austenitic manganese steel using jaw crusher tests with gravel, revealing that the introduction of three-body wear significantly increased material loss, with notable differences in wear quantities. These findings underscore the necessity for systematic studies on ZGMn13's response to diverse conditions.

Recent advances in tribology have highlighted the importance of surface topography and subsurface deformation in wear resistance. The Y.H. Wen research team [12]systematically explored the deformation response mechanisms of ZGMn13 under impact loading to address the insufficient work-hardening performance and excessive initial deformation of traditional high manganese steel under low loads. Experimental data demonstrated that compared to conventional high manganese steel, this alloy exhibits

significantly enhanced work-hardening rates during both low-strain (initial deformation) and high-strain (plastic deformation) stages. Li Jie [13] conducted a systematic study on three alloys Mn13, Mn13-2, and Mn18-2 using metallographic microscopy, scanning electron microscopy (SEM), and transmission electron microscopy (TEM) to elucidate the hardening mechanisms of high manganese steel under impact-abrasive wear. The experiments revealed ε-martensitic phase transformation and nanoscale mechanical twin structures in the subsurface layers of all specimens. The material's hardness enhancement primarily originated from the phase transformation strengthening effect of ε-martensite, while differences in hardening levels among materials correlated closely with the distribution density and morphological characteristics of mechanical twins. The study confirmed that mechanical twinning synergistically contributes to material strengthening through grain refinement and dislocation motion hindrance. However, the interaction between such microstructural evolution and environmental factors remains unclear. For instance, in sand-containing environments, hard abrasive particles may suppress strain hardening by inducing severe surface damage, thereby counteracting the material's inherent advantages. Conversely, water cooling might mitigate thermal softening effects during high-energy impacts, preserving the austenitic matrix. Resolving these conflicting hypotheses requires experimental validation under controlled conditions.

This study aims to address these gaps by systematically evaluating the impact and wear characteristics of ZGMn13 under dry, water-lubricated, and sand-abrasion conditions. Specific objectives include: (1) quantifying wear rates and surface hardening responses under varying impact energies, (2) characterizing wear mechanisms via SEM and 3D profilometry, (3) establishing correlations between environmental media, microstructural evolution, and tribological performance. To ensure methodological rigor, a custom-designed impact-wear tester was employed to simulate industrial conditions with controlled media injection.The experimental setup allows precise adjustment of impact energy and media flow rates for parametric analysis of wear behavior.

The significance of this work lies in its potential to guide material selection and design for ZGMn13 components facing multiphase wear challenges. For example, ore crushers operating in arid regions may experience significantly reduced component lifetimes due to sand intrusion under high-impact loads. By clarifying ZGMn13's degradation patterns under such conditions, this study provides actionable insights for alloy modification or surface treatment strategies. Furthermore, the findings contribute to a broader understanding of the tribological behavior of metastable austenitic steels, bridging the gap between laboratory-scale experiments and industrial service environments.

2. Test Details

2.1. Test Materials

Steel containing 11%-18% manganese is referred to as high-manganese steel, which represents the optimal choice for wear-resistant materials subject to strong impacts and high-pressure abrasive wear. In this work, we utilized the plow blade component from a 1K-30 model suspended chain-type trencher (Fig.1), where the plow blade material is ZGMn13 high-manganese steel and the clamping section consists of standard steel material GCr15, with their primary chemical compositions detailed in Table 1. Based on the operational requirements of the impact testing machine, the test specimen was fabricated from water-toughened high-manganese steel processed into a 10 × 10 × 30 mm^3 rectangular prism. The mechanical properties of the material are as follows: yield strength is 416 MPa, tensile strength is 970 MPa, and hardness is 293 HBW. While the down sample was manufactured from bearing steel into a hollow cylindrical configuration with an outer diameter of 50 mm, inner diameter of 30 mm, and width of 20 mm. The dimensional specifications and structural details of the specimens are illustrated in Fig.2.

2.2. Test Equipment

To more accurately investigate the friction and wear behavior of high-manganese steel materials under different impact conditions, a testing machine capable of simulating multiple working conditions was employed. This machine can be used to test the wear resistance of metallic materials under conditions such as impact or non-impact loading, contact or non-contact, and sliding or rolling friction, with metal materials interacting with various dry or wet abrasives. Through testing, quantitative measurements can be made of the wear on metallic materials under different loads and interaction modes, as well as experimental studies on wear mechanisms. The schematic diagram of the friction testing apparatust is detailed in Fig.3. The setup consists of an MLD-10 Load Abrasive Wear Testing Machine (referred to as Testing Machine A) and three core components: an impact test loading device (B), a computer control system (C), and a water injection system (D).

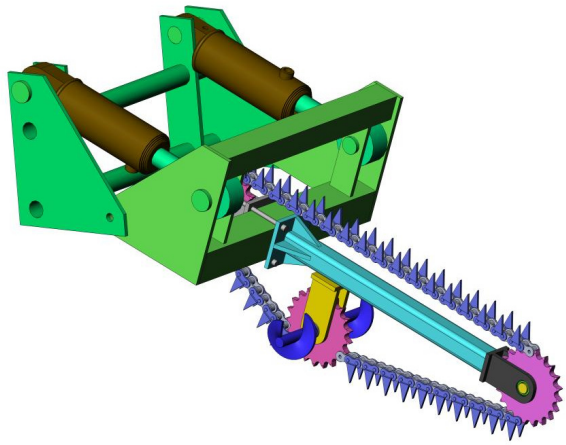

Figure 1. Structure of the 1K-30 model suspended chain-type trencher.

Table 1. Chemical Composition of Plow Blade/Clamping Section (w t/%)

Element	ZGMn13	GCr15
Fe	86.218	96.869
C	0.96	1.02
Si	0.41	0.24
Mn	12.4	0.37
P	0.012	0.018
Cr	–	1.47
S	–	0.013

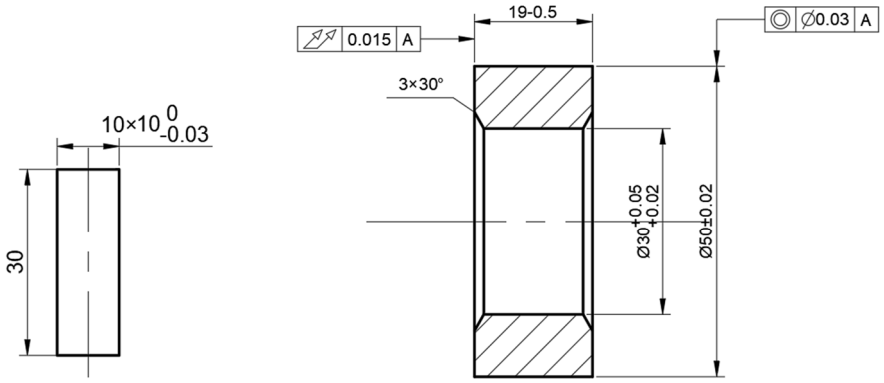

(a)Upper specimen (b) Lower specimen

Figure 2. Structure of the experimental sample (unit: mm)

The motor drives the large gear (19) through a pinion, causing the lower main shaft to rotate. A down sample is installed at the right end of the lower main shaft (13), with rubber washers forming a square groove on both sides of the down sample, allowing abrasives to pass through the groove. A pulley (18) is mounted on the left end of the large gear (19), which drives the upper main shaft pulley (16) via a V-belt to rotate the upper main shaft. An eccentric wheel is installed at the right end of the upper main shaft, which lifts the impact hammer through the eccentric wheel, enabling the hammer to perform reciprocating free-fall motion to achieve impact loading. The experimental procedure is as follows: First, press the main power switch button (1) to illuminate the stop indicator light (9), indicating that the control power is connected. Then operate the counter (2) to set the number of impacts. Before starting the counter, reset all digits to "0" by gently pressing the left reset button of the counter. To display impact counts, lightly press the count button to set the number, with the shift button below allowing adjustment of different digit values. After setting, wait until all digits of the impact counter display "0" before proceeding, or alternatively preset impact counts by first resetting the Timer (3) using the reset button on the time relay, then set the number via the count button with digit adjustments using the shift button. When starting the test, the machine will automatically stop once the time relay reaches the preset value. During testing, insert the hand pin into the hammer screw hole, lift the impact hammer (15), secure the safety pin, install the selected specimen clamp rod (12) to the lower end of the hammer, mount the lower specimen and tighten the lower specimen nut (20), then install the upper specimen with a latch. Calculate the drop height H (mm) based on the selected impact energy Ak, see formula (1) for details:

$$H = \frac{AK}{P}(mm) \tag{1}$$

Where Ak is the predetermined value and P is the hammer weight of 100 newtons. Locate the corresponding H value on the hammer calibration line, then adjust the specimen clamp rod in or out of the hammer until the required calibration line aligns with the machine's upper plane. Align the upper specimen and tighten both nuts(20) on the clamp rod. The impact energy is now set as required. Lift the hammer, remove the safety pin and hand pin to allow contact between upper and lower specimens. Load abrasives of different particle sizes into the sand hopper (10) for uniform flow to the working area. The control gate (11) with calibration lines inside the hopper regulates flow rate through adjustment screws. According to the experimental conditions, a water injection system (D) has been designed, which is composed of a water storage tank (14), infusion tubes, and a shut-off valve (17) with controllable flow rate. Select forward or reverse rotation as needed: press forward start button (8) for forward rotation, or for reverse rotation, first remove the V-belt (19), release the safety pin on forward and reverse switch (6), then press reverse button (7) to initiate counter-rotation operation.

2.3. Materials and Methods

As a major agricultural country, China must prioritize agricultural modernization to build a strong agricultural sector. However, influenced by complex terrain and agricultural economic structures, the development of agricultural mechanization in China exhibits differentiated characteristics.

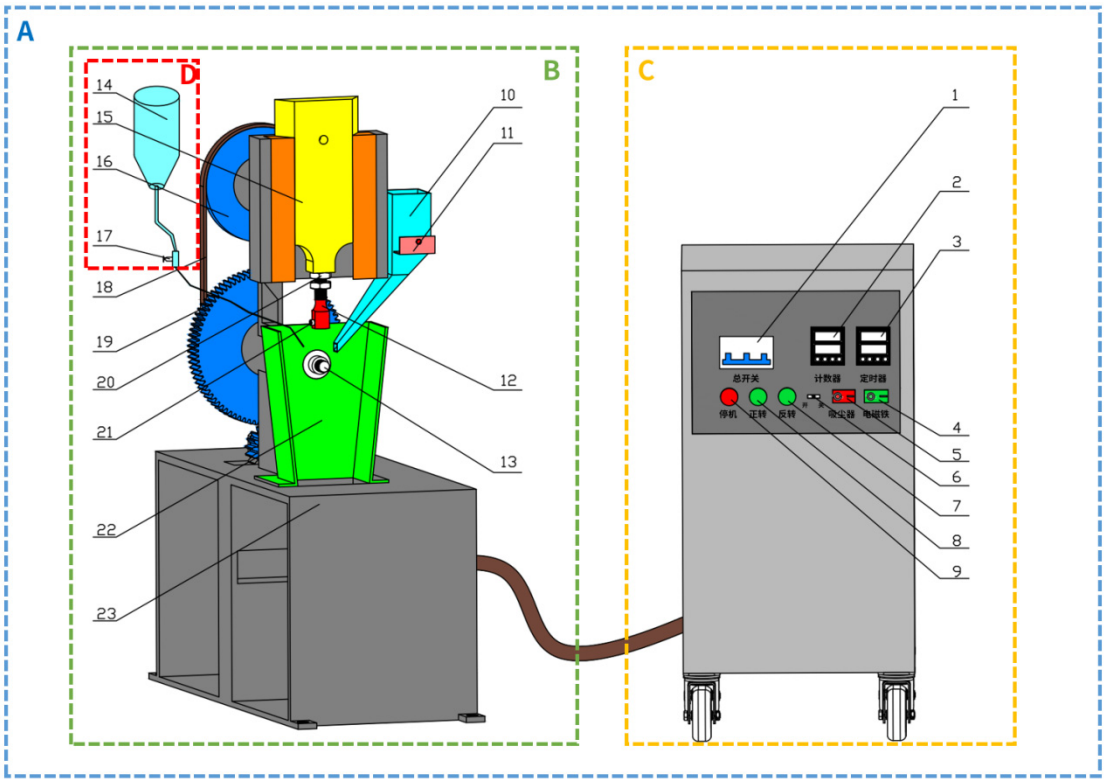

Figure 3. (A) MLD-10 Load Abrasive Wear Testing Machine; (B) Impact Test Loading Device ; (C) Computer Control System; (D) Water Injection System; 1: Main Power Switch Button; 2: Counter; 3: Timer; 4: Solenoid Switches; 5: Vacuum Cleaner Switch; 6: Forward and Reverse Switch; 7: Reverse Button; 8: Forward Start Button; 9: Stop Indicator Button ; 10: Sand Hopper; 11: Control Gate; 12: Specimen Clamp Rod; 13: Lower Main Shaft; 14: Water Injection System ; 15: Impact Hammer ; 16: Upper Main Shaft Pulley; 17: Shut-off Valve; 19: V-belt; 20: Nut;21: Latch;22: Sand Baffles;23: Pedestal.

This experiment investigates the impact friction and wear between plow blade components and fixtures under dry and wet conditions through nine test environment parameter groups. The impact energy was set at 1J, 2J, and 3J, corresponding to drop hammer heights of 10mm, 20mm, and 30mm respectively. Three experimental conditions were conducted: dry tests, sand-added comparative tests, and water-wetted comparative tests. For the sand-added group, quartz sand particles with mesh sizes of 100, 325, and 1000 were mixed in a 1:2:1 ratio. The abrasive flow rate was controlled at 25 cm^3/min, with abrasives introduced through a funnel adjacent to the down sample to simulate extreme dry wind-sand environments by scouring the surfaces of both test specimen and down sample. The water-moistened group maintained continuous wetting of specimens through purified water injection at 100 ml/min to replicate working conditions in paddy fields.The actual working status is as shown in the Fig.4. Each test lasted 3600 seconds under rolling contact with impact loading, and all experiments were repeated three times. Detailed experimental parameters are listed in Table 2.

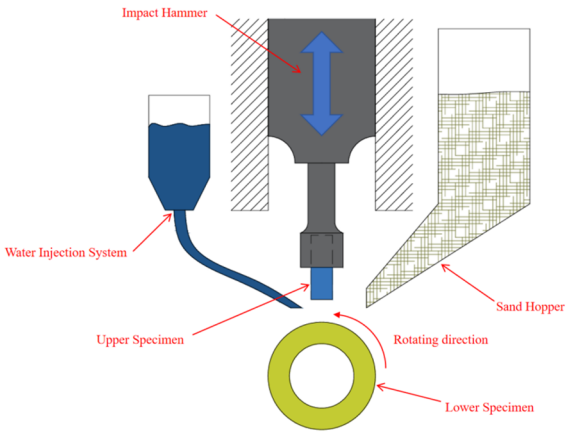

Figure 4. The actual working status

Table 2. Test parameters (repeated three times for each group).

Number	Test Impact/J	Friction medium	Test speed/times/min	Test time/s	Contact Form
1-1	1	/	200	3600	**Continuous**
1-2	2				
1-3	3				
2-1	1	Sand	200	3600	
2-2	2				
2-3	3				
3-1	1	Water	200	3600	
3-2	2				
3-3	3				

2.4. Test Process and Analysis Method

The experimental sample preparation process is as follows: First, high-manganese steel and bearing steel specimens were progressively ground using #60, #240, #400, #600, #1000, and #1500 grit sandpapers. Subsequently, polishing was performed with W1.5, W1.0, and W0.5 polishing pastes to eliminate surface micro-defects and ensure effective contact between friction pairs. Post-surface treatment, specimens underwent 15-20 minutes of ultrasonic cleaning in ethanol medium, followed by blow-drying with a hair dryer and fixation using needle fixtures in a constant-temperature drying oven for 6-hour dehydration. All operations employed tweezers to prevent contamination. Mass measurement utilized a precision balance (JA 4103, accuracy of 0.001g , China), with each specimen measured five times independently to obtain an arithmetic mean as the initial mass baseline. During experimental setup preparation: 10# mechanical oil was injected into the upper/lower oil cups and the ram pressure plate oil chamber. After confirming the main drive gear rotation direction, specimens were installed. For specific test conditions: the sand-containing medium group required pre-loading of standard test sand into the metering funnel, adjusting sand flow rate via the baffle opening; the water medium group required configuration of a constant-flow water supply system. The test program commenced after parameter configuration. Post-experiment, specimens were cooled to room temperature before disassembly. The standardized cleaning (15-20 min ultrasonic cleaning) and drying protocols were repeated. Final mass determination followed the same five-measurement protocol to calculate mass loss for subsequent tribological performance analysis.

After the test, both the test specimen and down sample exhibited significant deformation, with varying degrees and forms of surface wear. A spectral confocal 3D profilometer (VS-TA 2, Shanghai Vision Technology Co., Ltd., China) was then employed to observe the 3D morphology of the worn surfaces and measure surface deformation and roughness. The surface damage of the specimens was analyzed using a scanning electron microscope (KYKY-EM 6X00, Beijing Zhongke Technology Co., Ltd., China) and an ultra-depth-of-field optical microscope (SM-5000, Shanghai SXian Optoelectronics Co., Ltd., China). To further investigate the material's impact performance, a diamond wire cutting machine was used to section the worn specimens along the rotational direction of the down sample. Subsequently, the cut surface was ground and polished, and then the hardness distribution characteristics of the impact wear-hardened layer were measured using a microhardness tester (Shanghai Yanrun Optical Machine, HVS-1000). Due to the exceptionally rough wear surface, hardness testing was performed starting from a depth of 50 μm below the surface. Measurements were taken at intervals of 50–100 μm, with six points measured in total. The average hardness was calculated from these measurements.

3. Result

3.1. Wear Rate

Fig. 5 details the effects of different impact energies and media environments on the weight loss of the test specimen (ZGMn13). In the dry control group (Fig.5a), the upper specimen exhibited maximum wear of approximately 7.54 mg at 1J impact energy, while showing minimum wear of 1.46 mg at 3J. The weight loss of the test specimen decreased with increasing impact energy, consistent with previous findings by Ge et al. [14-15] regarding the work toughening and strain-hardening characteristics of high-manganese steel. Notably, as shown in Fig.5b (sand-containing group), the introduction of mixed-granularity quartz sand significantly amplified wear in both specimens. The most pronounced difference occurred at 1J impact energy, where the sand-containing group showed approximately 18-fold higher mass loss compared to the dry group. At 3J impact energy, this amplification reduced to about 11-fold. Both test groups maintained the decreasing weight loss trend with increasing impact energy for high-manganese steel. Interestingly, Fig.5c (water-containing group) revealed an inverse relationship where the high-manganese steel's weight loss increased with impact energy - contrasting with both dry and sand-containing groups. Among all three environmental conditions, the water-containing group exhibited the least material loss (followed by the dry group), while the sand-containing group showed the most severe wear.

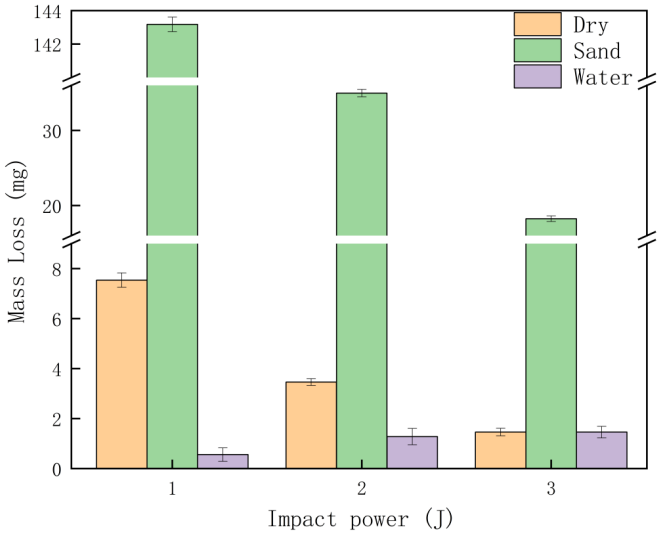

Figure 5. The weight loss of the test specimen and down specimen in different impact energies and media environments. (a) Dry group; (b) Sand-containing group; (c) Water-containing group

3.2. Hardness

This study reveals the complex coupling relationship between the wear behavior and hardening response of ZGMn13 high manganese steel under different impact energies and environmental media. The hardness of the impact wear hardening layer was measured using a microhardness tester (Shanghai Yanrun Optics and Machinery, HVS-1000). Due to the abnormally rough wear surface, hardness measurements were taken starting from a depth of 50 μm below the surface, with measurements taken every 50 to 100 μm, totaling six points. The specific data are presented in Fig.6.In the dry friction control group, hardness demonstrates a linear increase with rising impact energy: average hardness values reach 352 HV, 423 HV, and 498 HV under 1J, 2J, and 3J impacts respectively. This progression aligns with the material's work hardening characteristics. Low-energy impacts (1J) induce only localized plastic deformation with limited dislocation density, whereas 3J impacts significantly strengthen the matrix through dynamic strain aging and martensitic transformation [13, 16], achieving a 41.5% hardness enhancement.

In the sand-containing group, the average hardness at 1J impact measures 285 HV, markedly lower than the control group's 352 HV, indicating that quartz sand particle embedding and surface fragmentation suppress initial hardening effects. However, as impact energy increases to 3J, the hardness recovers to 410 HV, approaching the control group's 2J level (423 HV). This recovery mechanism stems from energy-driven sand particle refinement and more pronounced strain accumulation under high-energy impacts [16], which partially counteracts the abrasive damage.

The water-lubricated group displays fundamentally different hardness behavior from both dry and abrasive conditions. Average hardness values remain stable within 315-335 HV across 1J-3J impacts, showing no significant energy dependence. The lubricating water film reduces direct mechanical strengthening contributions while hydrogen permeation and localized electrochemical corrosion induce microstructural weakening [10, 17]. Notably, the 3J impact in aqueous conditions exhibits substantial hardness fluctuations, reflecting the competitive mechanism between brittle spalling induced by cavitation bubble collapse and passive film regeneration processes.

In summary, the 50μm depth hardness data reveal three distinct mechanisms: 1) Dry friction enables significant wear resistance improvement through phase transformation-twinning synergy under high-energy impacts; 2) Abrasive environments achieve hardness recovery via energy-dependent particle refinement and strain accumulation; 3) Aqueous media suppress the material's inherent hardening potential by inhibiting plastic deformation while introducing corrosive damage.

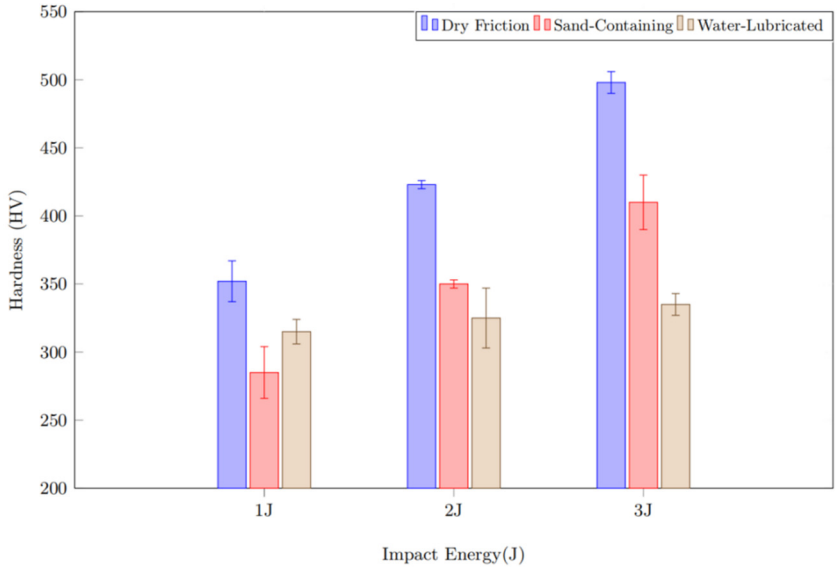

Figure 6. The hardness of ZGMn13 high-manganese steel samples at 1J, 2J, and 3J under different working conditions

3.3. Surface Contouring and Wear

Fig.7-8 demonstrate the surface morphology and wear patterns of ZGMn13 high manganese steel material under different impact energies in the control group, and when quartz sand and water were added respectively. In the control group, the sample surface showed the most severe morphological damage at 1J impact energy, characterized by numerous deep and wide craters (Fig.8a). This resulted in significant delamination craters, adhesive wear, and large-volume spalling debris on the sample surface (Fig.7a-b). With increasing impact energy, the work hardening and impact toughness of ZGMn13 high manganese steel were enhanced, leading to gradually reduced surface deformation (Fig.8b-c). At 2J impact energy, the crater area diminished while the volume of impact-induced spalling debris increased (Fig.7c-d). When the impact energy reached 3J, the sample surface became smoother with prominent plough grooves and indentations (Fig.7e), accompanied by more extensive spalling fragments due to the elevated impact energy (Fig.7f).

After adding the mixed quartz sand particles into the simulated wind-sand environment, the surface damage of the specimens was mainly characterized by plowing grooves, abrasive wear, spalling, and adhesive wear (Fig. 9a-f). Compared to the control group specimens under the same impact energy, the surface roughness increased and the surface deformation became more severe (Fig. 10a-c). SEM observations revealed that under 1J impact energy, quartz sand particles created deep and elongated plowing grooves on the specimen surface (Fig. 9a-b). At 2J impact energy, numerous short and dense plowing grooves caused by

spalling debris and micro-plowing of quartz sand particles were observed. When the impact energy increased to 3J, the wear loss significantly decreased, with a sharp reduction in the number of plowing grooves. The surface damage mainly manifested as adhesive wear and spalling. Notably, under 1J and 2J impact energies, insufficient surface hardening allowed quartz particles to embed into the specimen, forming concentrated

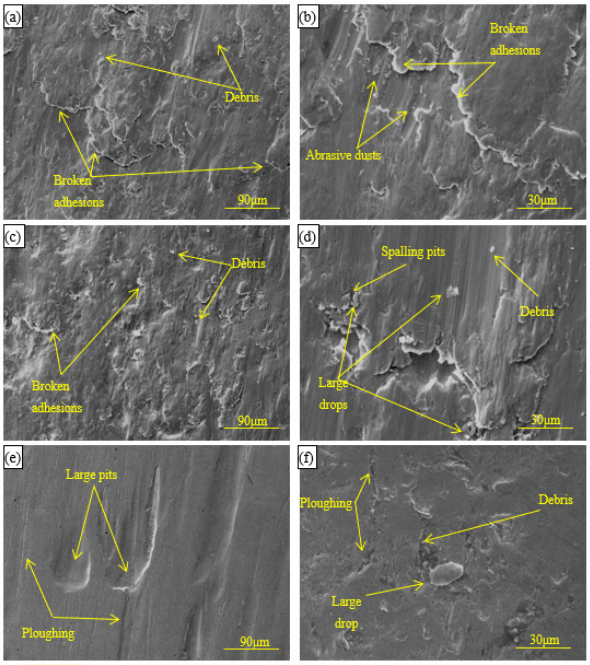

Figure 7. The SEM micrographs of the wear surface of the ZGMn13 high-manganese steel samples in the dry group under different impact energy levels. (a-b)1J;(c-d)2J;(e-f)3J

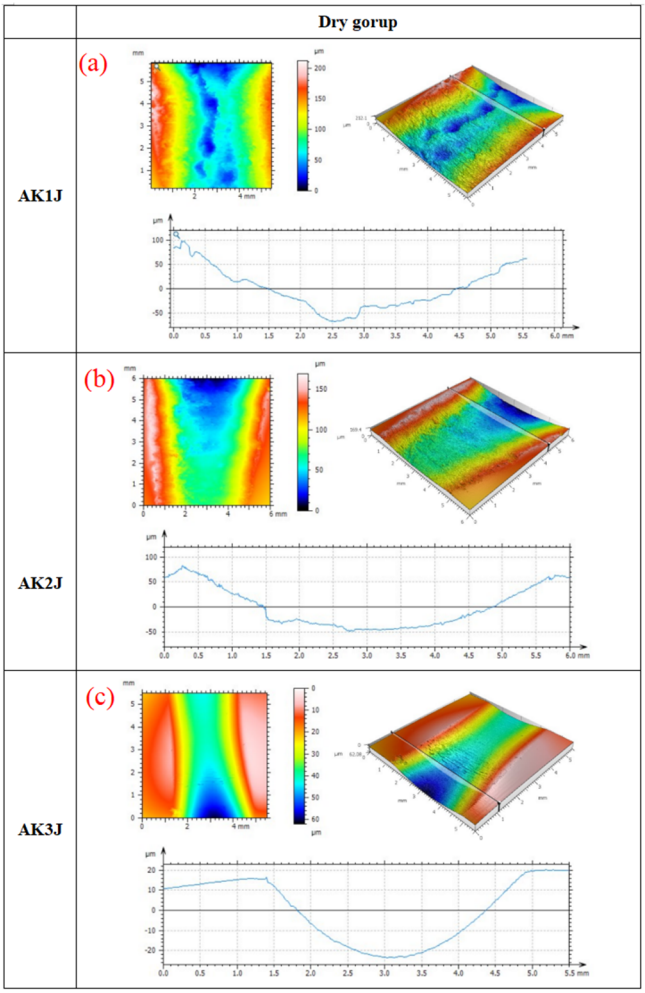

Figure 8. Three-dimensional surface profiles of the wear surface of ZGMn13 high-manganese steel samples in the dry group under different impact energy levels. (a)1J;(b)2J;(c)3J

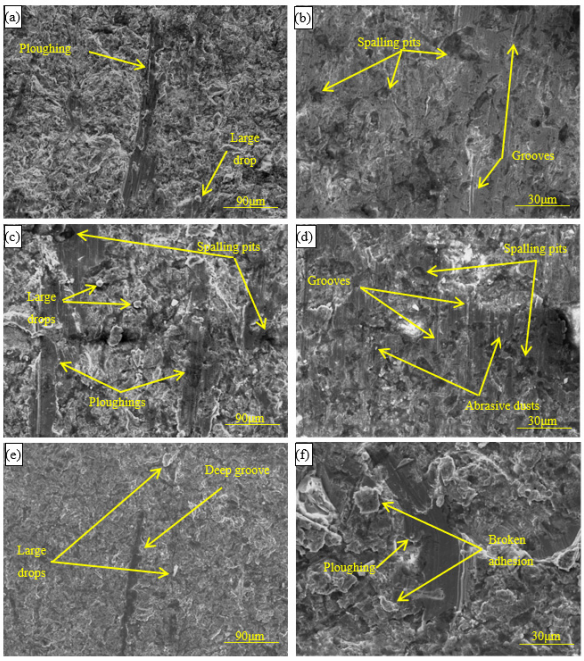

Figure 9. The SEM micrographs of the wear surface of the ZGMn13 high-manganese steel samples under sand conditions at different impact energy levels. (a-b)1J;(c-d)2J;(e-f)3J

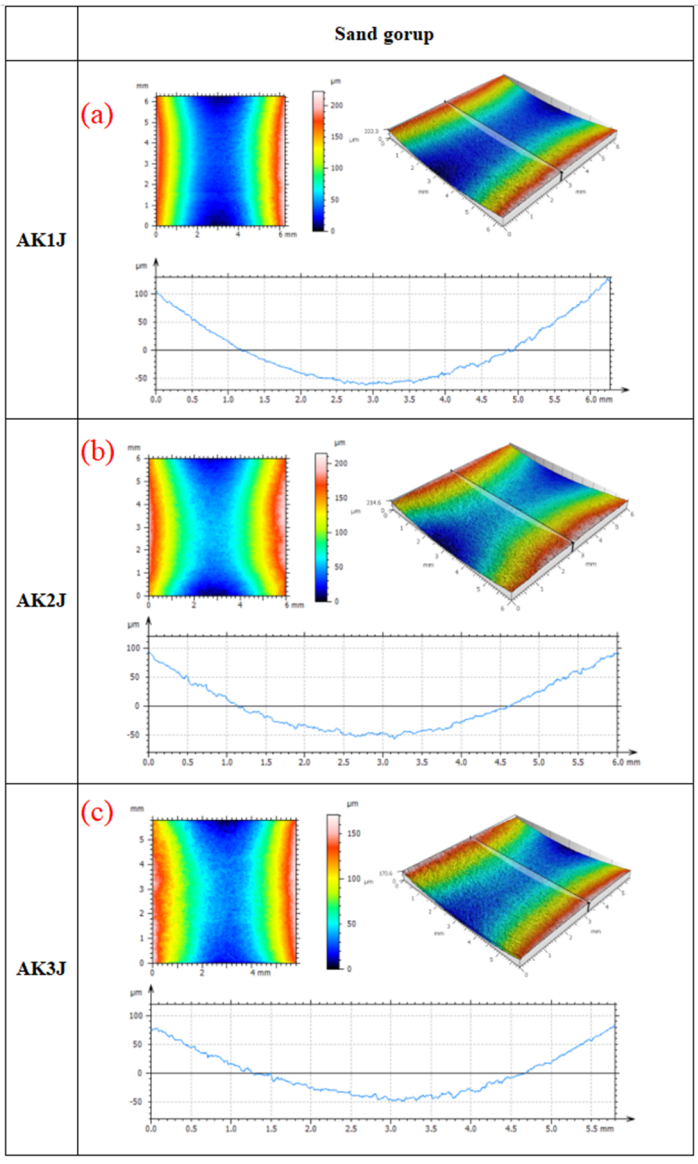

Figure 10. Three-dimensional surface profiles of the wear surface of ZGMn13 high-manganese steel samples under sand conditions at different impact energy levels. (a)1J;(b)2J;(c)3J

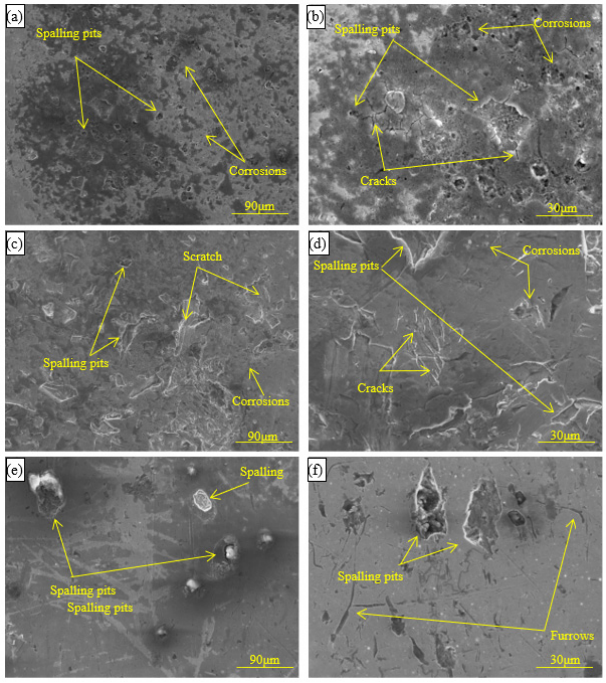

Figure 11. The SEM micrographs of the wear surface of the ZGMn13 high-manganese steel samples under water conditions at different impact energy levels. (a-b)1J;(c-d)2J;(e-f)3J

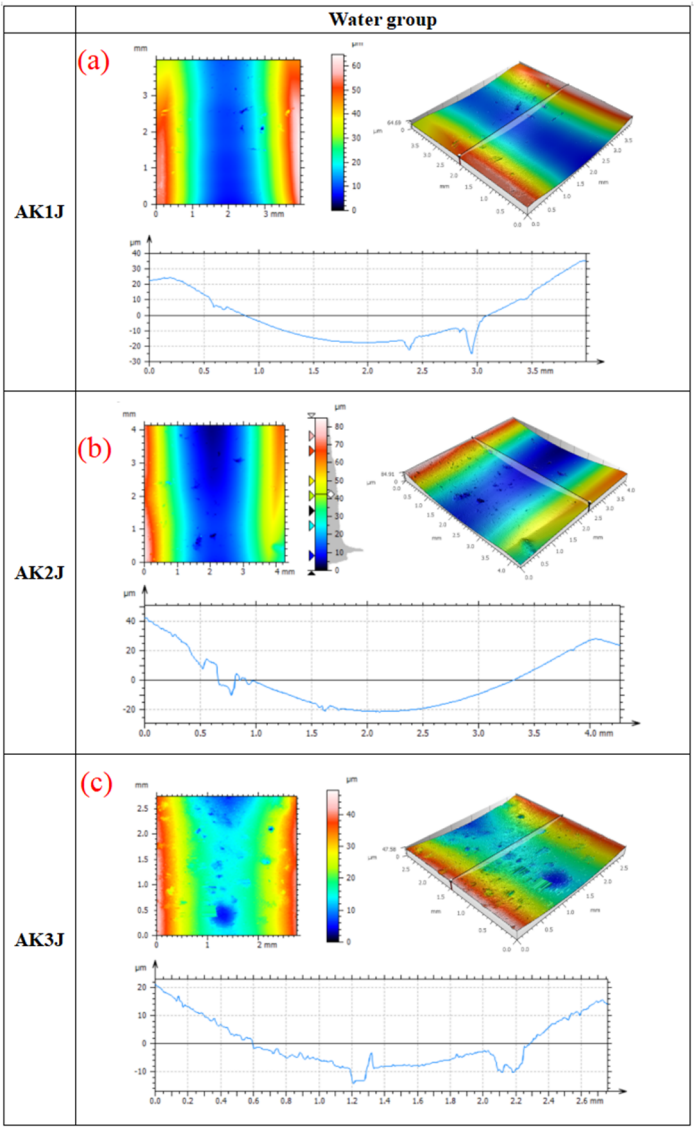

Figure 12. Three-dimensional surface profiles of the wear surface of ZGMn13 high-manganese steel samples under water conditions at different impact energy levels. (a)1J;(b)2J;(c)3J

Stress fields that generated dense micro-pits (Fig. 9a-d). Under 3J impact energy, fractured quartz particles participated in the impact process. The secondary microcracks thus generated preferentially propagated along austenite grain boundaries, forming a unique scaly layered morphology (Fig. 9e-f).

When water medium was introduced, the wear behavior of ZGMn13 high manganese steel demonstrated a unique corrosion-wear synergistic effect. The surface morphology transitioned from adhesive-dominated wear in the control and sand-added groups to extensive crack networks and large-scale spalling. Notably, the water-added samples exhibited the least surface deformation (Fig.11-12), attributable to sufficient lubrication during contact enabled by water. Under 1J impact energy, lubricating water films triggered localized electrochemical corrosion, resulting in densely distributed pitting craters (152 pits/mm^2,Fig.11a). Cracks nucleated at the crater base and propagated along twin boundaries, while honeycomb-like erosion patterns emerged (Fig.11b). At 2J impact energy, intensified dynamic water-wedging effects promoted hydrogen aggregation at crack tips, forming hydrogen-induced crack networks (Fig.11c). Simultaneously, impact-induced dislocation motion facilitated cyclic rupture/regeneration of passivation films , generating densely clustered spalling features (Fig.11d). When impact energy reached 3J, high-pressure waterjet effects induced turbulent cavitation erosion. The surface developed hydrogen bubble collapse pits (5-8 μm diameter, Fig.11e-f), with pit depth-to-diameter ratios increasing from 0.8 (1J) to 1.6 (3J) through three-dimensional profilometry. Electrochemical monitoring revealed transient current density peaks up to 1.2 mA/cm^2 during impacts, confirming mechano-electrochemical acceleration of material degradation.

4. Discussion

This study reveals the complex coupling relationship between wear behavior and hardening response of ZGMn13 high manganese steel under different impact energies and environmental media, and it's impact wear mechanism is shown in Fig13. Under dry friction conditions, low impact energy (1J) results in insufficient plastic deformation, leading to low surface dislocation density, restricted martensitic phase transformation and mechanical twinning formation, with surface hardness only reaching 352 HV. At this stage, wear primarily manifests as adhesive wear and bulk spalling. When impact energy increases to 3J, dynamic strain aging effects significantly enhance, with substantial increases in dislocation multiplication and twin density, causing surface hardness at 50μm depth to surge to 498 HV (41.5 % improvement). The high-density martensitic structure not only hinders crack propagation but also minimizes wear loss (1.46 mg). This phenomenon confirms the core mechanism of "impact energy-driven hardening" in high manganese steel, consistent with findings by Liu et al. [16-19], where energy input achieves strengthening through plastic strain-induced phase transformation and microstructural refinement.

In sand-containing groups, the introduction of quartz sand alters the dominant wear mechanism. After abrasive action, worn areas become more prone to spalling, leading to more significant material mass loss. This mechanically induced material removal mechanism exacerbates mass reduction in damaged regions [20]. Under 1J impact, sand particle embedding creates stress concentration zones, causing surface fragmentation and hardness plummet to 285 HV. At this stage, three-body abrasive action from sand particles induces severe plowing wear and micro-pit formation. However, when impact energy increases to 3J, sand particles fracture into fine grains under intense impact. These fine particles promote secondary twinning and local strain fields through dislocation pinning effects, restoring surface hardness to 410 HV (approaching 2J level in blank group) [19]. This result indicates that high-energy impacts can partially counteract abrasive damage through "sand refinement-strain strengthening" synergy, though overall wear remains significantly higher than dry friction conditions (11 times the blank group).

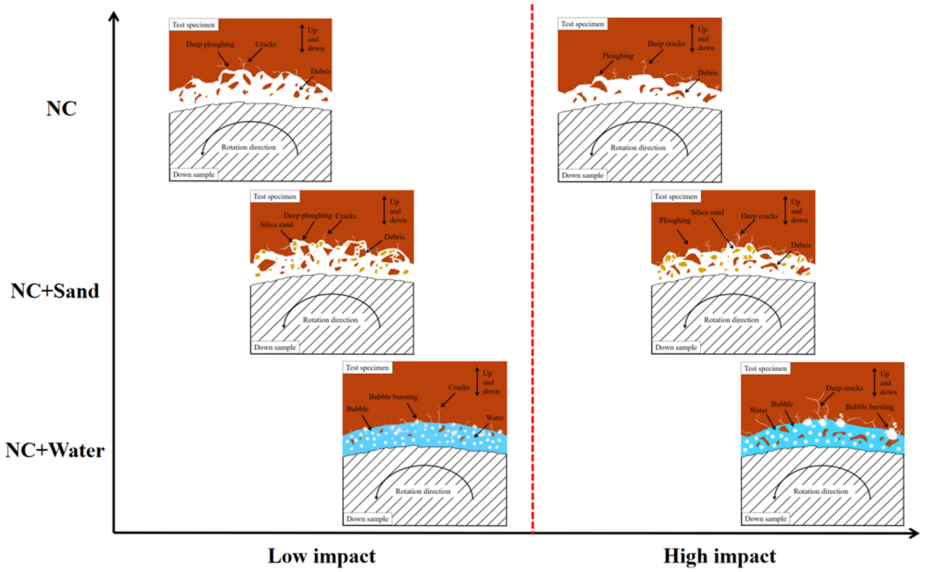

Figure 13. The impact wear mechanism of ZGMn13 high manganese steel under different impact energies and environmental media

The water-lubricated group demonstrates unique corrosion-mechanical synergistic effects. Although water film lubrication reduces direct mechanical deformation, the introduction of water medium induces hydrogen penetration and electrochemical corrosion [21], while the impact between the two interfacial phases creates localized low pressure

leading to water vaporization and cavitation bubble formation. The collapse of these bubbles releases energy, resulting in pitting on the material surface as shown in Fig. 10. This surface morphology aligns with Krella's findings on cavitation erosion and cavitation phenomena [22,23]. Under 3J impact, the increased impact energy directly causes brittle spalling due to localized stress from bubble collapse. Although the water medium inhibits hardening dominated by plastic deformation, the cumulative effect of corrosion damage causes the wear rate to increase with impact energy, showing an opposite trend compared to the dry friction and sand particle groups.

5. Conclusion

1. Impact Energy and Hardening Response: The wear resistance of ZGMn13 significantly improves with increasing impact energy. Under 3J impact, hardness reaches 498 HV (41.5% increase compared to 1J), primarily attributed to synergistic strengthening from martensitic phase transformation, mechanical twinning, and gradient hardening layers[24-26].

2. Dual Effects of Environmental Media: In sand environments, 1J impact causes abrasive particle embedding leading to hardness reduction (285 HV) and severe plowing wear[11]. However, 3J impact partially restores hardness (410 HV) through sand particle refinement-induced secondary twinning[7]. In water media, lubrication suppresses plastic hardening (hardness stabilizes at 315-335 HV), but hydrogen embrittlement and cavitation corrosion increase wear rate [22, 23].

3. Mechanism Competition and Engineering Implications: In dry/sandy environments, high-energy impacts dominate wear control through strain hardening. Water environments require prioritized corrosion damage mitigation. ZGMn13 demonstrates inherent advantages for high-impact sandy conditions, while water-exposed components demand anti-corrosion coatings or low-carbon-equivalent alloy design.

The wear performance of ZGMn13 high manganese steel is critically governed by environmental modulation of its hardening mechanisms: under dry friction conditions, the synergistic combination of high-impact energy (3J) and phase transformation strengthening maximizes material potential, achieving 498 HV hardness through martensitic transformation and mechanical twinning, whereas in sandy environments, abrasive particle refinement under 3J impact triggers secondary twinning and strain accumulation[11], partially restoring hardness to 410 HV despite initial sand-induced degradation at 1J. In contrast, water-mediated corrosion mechanisms override mechanical advantages, as stabilized hardness (315-335HV) from lubrication is counteracted by hydrogen embrittlement and cavitation erosion, leading to energy-dependent wear escalation. These findings establish an environment-stratified selection framework-prioritizing ZGMn13 for arid, high-impact applications like mining machinery while mandating corrosion-resistant coatings or alloy modifications for aqueous service environments.

References

[1] L.R. Jeckins, R.D. Forrest, Properties and selection: irons, steels, and high-performance alloys, Metals Handbook, 1993.

[2] Y.H. Wen, H.B. Peng, H.T. Si, R.L. Xiong, D. Raabel., A novel high manganese austenitic steel with higher work hardening capacity and much lower impact deformation than Hadfield manganese steel, Materi-als & Design, 55, 798-804, 2014, 10. 1016/j. matdes.2013.09.057.

[3] C. Chen, F.C. Zhang, F. Wang, H Liu, B.D. Yul., Effect of N plus Cr alloying on the microstructures and tensile properties of Hadfield steel, Materials Science & Engineering, A. Structural Materials: Properties, Misrostructure and Processing, 679- 679, 2017.

[4] D.V. Lychagin, A.V Filippov,O.S. Novitskaia, Y.I. Chumlyakov, E.A. Kolubaev, O.V. Sizova, Friction-induced slip band relief of -Hadfield steel single crystal oriented for multiple slip deformation, Wear, 2017, 10.1016/j.wear. 2016. 12.028.

[5] B. Hutchinson, N. Ridley, On dislocation accumulation and work hardening in Hadfield steel, Scripta Materialia, 55, 4, 299-302, 2006, 10.1016/j.scriptamat.2006.05.002.

[6] C. Efstathiou, H. Sehitoglu, Strain hardening and heterogeneous defor-mation during twinning in Hadfield steel, Acta Materialia, 58, 5, 1479-1488, 2010, 10.1016/j. actamat. 2009. 10.054.24

[7] Y.H. Xu, S.L. Yuan, Q.Y. Luo, Study on the Wear Mechanism of High Manganese Steel under High-Energy Impact Contact Loads, Hot Work-ing Technology, 1, 10-12, 2000, (in Chinese).

[8] Q. Fang, Z. Wang, C. Chen, X. Zhang, X. Feng, Y. Li, Z. Yang, F. Zhang, Multistage Dynamic Damage and Microstructural Evolution of High-Manganese Steel under Rolling-Sliding Contact Conditions, Wear, 2025, 205994.

[9] H. Fu, P. Chen, X. Huang, W. Zhang, R. Wang, Q. Huang, Q. Shan, Effect of N and aging treatment on precipitation behavior, mechanical properties and wear resistance of Ti–V–Nb alloyed high manganese steel, Journal of Materials Research and Technology, 29, 1949-1961, 2024.

[10] X. Liang, J. Yan, C. Li, X. Lou, X. Dong, R. Wang, Water lubrication friction and wear behaviors of WC hard alloy and metal pairs, Wear, 2025, 205795.

[11] P.C. Machado, J.I. Pereira, A. Sinatora, Abrasion wear of austenitic manganese steels via jaw crusher test, Wear, 476, 203726, 2021.

[12] Y.H. Wen, H.B. Peng, H.T. Si, R.L. Xiong, D. Raabe, A novel high manganese austenitic steel with higher work hardening capacity and much lower impact deformation than Hadfield manganese steel, Materials & Design, 55, 798-804, 2014.

[13] J. Li, L. Xu,Y. Feng, S. Wu, W. Li, Q. Wang, P. Zhang, X. Tu, Hardening mechanism of high manganese steel during impact abrasive wear, Engineering Failure Analysis, 154, 107716, 2023.

[14] S. Ge, Q. Wang, J. Wang, The impact wear-resistance enhancement mechanism of medium manganese steel and its applications in mining machines, Wear, 376, 1097-1104, 2017.

[15] O.A. Zambrano, A general perspective of Fe–Mn–Al–C steels, Journal of materials science, 53, 20, 14003-14062, 2018.

[16] W. Liu, T. Jiang, S. Wei, L. Xu, C. Chen, H. Yu, X. Jin, H. Ding, C. Zhang, K. Pan, A comparative analysis of abrasive wear behaviors and mechanisms of pearlitic and carbide-free bainitic steels for grinding mill liners under varied impact loads, Wear, 2025, 205765. 25

[17] H. Engqvist, N. Ax´en, S. Hogmark, Tribological properties of a binderless carbide, Wear, 232, 2, 157-162, 1999.

[18] W. Yan,L. Fang, K. Sun, Y. Xu, Effect of surface work hardening on wear behavior of Hadfield steel, Materials Science and Engineering: A, 460, 542-549, 2007.

[19] B. Hutchinson, N. Ridley, On dislocation accumulation and work hardening in Hadfield steel, Scripta Materialia, 55, 4, 299-302, 2006.

[20] M. I. Clark, The influence of the squeeze film in slurry erosion, Wear, 256, 918-926, 2004.

[21] I. Karaman, H. Sehitoglu, K. Gall, Y.I. Chumlyakov, H.J. Maier, Deformation of single crystal hadfield steel by twinning and slip, Acta Materialia, 48, 1345-1359, 2000.

[22] A. K. Krella, A. Maurin, Z. Krzemianowski, Degradation of Armco iron caused by cavitation: Part II– Correlation with stress analysis, Engineering Failure Analysis, 128, 105621, 2021.

[23] Y. Li, L. Zhu, Y. Liu, Y. Wei, Y. Wu, D. Tang, Z. Mi, On the strain hardening and texture evolution in high manganese steels: Experiments and numerical investigation, Journal of the Mechanics and Physics of Solids, 61, 2588-2604, 2013.

[24] D. Ma, T. J. Harvey, Y. N. Zhuk, R.G. Wellman, J.K. Wood, Cavitation erosion performance of CVD W/WC coatings, Wear, 452, 203276, 2020.

[25] M. Sabzi, M. Farzam, Hadfield manganese austenitic steel: a review of manufacturing processes and properties, Materials Research Express, 6, 1065c2, 2019.

[26] J. Liu, X. Yao, Y. Li, L. Yang, Investigation of the generation mechanism of the internal pressure of metal thin-walled tubes based on liquid impact forming, The International Journal of Advanced Manufacturing Technology, 105, 3427-3436, 2019.